REPORT DOCUMENTATION PAGE

Form Approved OMB NO. 0704-0188

1. REPORT DATE (DD-MM-YYYY)	2. REPORT TYPE	3. DATES COVERED (From - To)
15-08-2018	Final Report	1-May-2015 - 30-Apr-2018

4. TITLE AND SUBTITLE
Final Report: Molecule-Surface Dynamics in Functionalized Mesoporous Silicon

5a. CONTRACT NUMBER
W911NF-15-1-0176

5b. GRANT NUMBER

5c. PROGRAM ELEMENT NUMBER
611102

6. AUTHORS

5d. PROJECT NUMBER

5e. TASK NUMBER

5f. WORK UNIT NUMBER

7. PERFORMING ORGANIZATION NAMES AND ADDRESSES
Vanderbilt University
PMB 407749
2301 Vanderbilt Place
Nashville, TN 37240 -7749

8. PERFORMING ORGANIZATION REPORT NUMBER

9. SPONSORING/MONITORING AGENCY NAME(S) AND ADDRESS (ES)
U.S. Army Research Office
P.O. Box 12211
Research Triangle Park, NC 27709-2211

10. SPONSOR/MONITOR'S ACRONYM(S)
ARO

11. SPONSOR/MONITOR'S REPORT NUMBER(S)
66677-CH.17

12. DISTRIBUTION AVAILIBILITY STATEMENT
Approved for public release; distribution is unlimited.

13. SUPPLEMENTARY NOTES
The views, opinions and/or findings contained in this report are those of the author(s) and should not contrued as an official Department of the Army position, policy or decision, unless so designated by other documentation.

14. ABSTRACT

15. SUBJECT TERMS

16. SECURITY CLASSIFICATION OF:			17. LIMITATION OF ABSTRACT	15. NUMBER OF PAGES	19a. NAME OF RESPONSIBLE PERSON
a. REPORT	b. ABSTRACT	c. THIS PAGE			Sharon Weiss
UU	UU	UU	UU		19b. TELEPHONE NUMBER 615-343-8311

RPPR Final Report
as of 01-Nov-2018

Agency Code:

Proposal Number: 66677CH **Agreement Number: W911NF-15-1-0176**
INVESTIGATOR(S):

Name: Sharon M Weiss
Email: sharon.weiss@Vanderbilt.Edu
Phone Number: 6153438311
Principal: Y

Organization: **Vanderbilt University**
Address: PMB 407749, Nashville, TN 372407749
Country: USA
DUNS Number: 965717143 EIN: 620476822
Report Date: 31-Jul-2018 Date Received: 15-Aug-2018
Final Report for Period Beginning 01-May-2015 and Ending 30-Apr-2018
Title: Molecule-Surface Dynamics in Functionalized Mesoporous Silicon
Begin Performance Period: 01-May-2015 **End Performance Period:** 30-Apr-2018
Report Term: 0-Other
Submitted By: Sharon Weiss Email: sharon.weiss@Vanderbilt.Edu
Phone: (615) 343-8311
Distribution Statement: 1-Approved for public release; distribution is unlimited.

STEM Degrees: 2 **STEM Participants:** 5

Major Goals: The primary goal of this project is to gain understanding of the impact of porous silicon functionalization chemistry and morphology on the surface interaction mechanisms involved in macroscopic diffusion and attachment of different chemical and biomolecular species in porous silicon films and membranes. In particular, we will seek to increase the state of knowledge in the following areas: 1) Effect of surface passivation layer on molecular and ionic diffusion through porous silicon films; 2) Effect of pore morphology, including closed-ended and open-ended pores, on diffusion rates; and 3) Diffusion and attachment dynamics and efficacy of molecular capture in porous silicon films functionalized for specific binding (e.g., DNA, peptide, antibody bioreceptors).

Accomplishments: Please see attached document.

Training Opportunities: During this 3-year program, two graduate students, three undergraduate students, and one postdoctoral researcher had the opportunity to participate in interdisciplinary research in the fields of material science, chemistry, electrical engineering, and physics. In particular, all participants gained expertise in nanomaterial fabrication, functionalization, and characterization. Furthermore, the graduate students and postdoctoral researcher gained skills in effective teaching practices through student mentoring and participation as members of teams engaged in STEM outreach.

RPPR Final Report
as of 01-Nov-2018

Results Dissemination: During the 3-year program, the results of this project were disseminated at conferences, in publications, and during outreach activities, as specified below.

Publications:

G. A. Rodriguez, P. Markov, A. P. Cartwright, M. H. Choudhury, F. O. Afzal, T. Cao, S. I. Halimi, S. T. Retterer, I. I. Kravchenko, S. M. Weiss, "Photonic crystal nanobeam biosensors based on porous silicon," Appl. Phys. Lett. Photon., in revision (2018).

T. Cao, Y. Zhao, C. A. Nattoo, M. H. Choundhury, and S. M. Weiss, "A smartphone biosensor based on analyzing structural color of porous silicon microcavity," manuscript in preparation (2018).

G. Gaur, S. Hu, R. L. Mernaugh, I. I. Kravchenko, S. T. Retterer, S. M. Weiss, "Label-free detection of Herceptin® using suspended silicon microring resonators," Sens. Act. B, in press (2018). doi: 10.1016/j.snb.2018.07.081

Y. Zhao, G. Gaur, S. T. Retterer, P. E. Laibinis, and S. M. Weiss, "Flow-through porous silicon membranes for real-time label-free biosensing," Anal. Chem. 88, 10940-10948 (2016). doi: 10.1021/acs.analchem.6b02521

Y. Zhao, G. Gaur, R. L. Mernaugh, P. E. Laibinis, and S. M. Weiss, "Comparative kinetic analysis of closed-ended and open-ended porous sensors," Nanoscale Res. Lett. 11, 395 (2016). doi: 10.1186/s11671-016-1614-3

T. Cao, Y. Zhao, and S. M. Weiss, "A smartphone compatible colorimetric biosensing system based on porous silicon," Proc. of SPIE 10077, 1007713 (2017). doi: 10.1117/12.2250659

Y. Zhao, G. A. Rodriguez, Y. M. Graham, T. Cao, G. Gaur, and S. M. Weiss, "Resonant photonic structure in porous silicon for biosensing," Proc. of SPIE 10081, 100810D (2017). doi: 10.1117/12.2256893

Yiliang Zhao, Engineering porous silicon photonic structures towards fast and reliable optical biosensing, Ph.D. Thesis, Vanderbilt University, May 2017.

Presentations:

T. Cao, Y. Zhao, C. A. Nattoo, and S. M. Weiss, "A smartphone biosensor based on colorimetric analysis of porous silicon filters," Porous Semiconductors – Science and Technology Conference, La Grande Mottte, France, Mar. 2018.

S. M. Weiss, "Exploiting light-matter interaction in silicon photonics for biosensing," Physics Department Seminar Series, University of Pavia, Pavia, Italy, Nov. 2017. (invited)

S. M. Weiss, "Exploiting light-matter interaction in silicon photonics for biosensing," IEEE Photonics Society Seminar Series, Sapienza University of Rome, Rome, Italy, Nov. 2017. (invited)

S. M. Weiss, "Nanostructured silicon optical biosensors: A versatile platform for molecular detection," Army Research Lab, Adelphi, MD, May 2017. (invited)

S. M. Weiss, "Exploiting light-matter interaction in silicon photonics for biosensing," IEEE Photonics Society Seminar Series, CREOL, College of Optics and Photonics, University of Central Florida, Orlando, FL, April 2017. (invited)

S. M. Weiss, "Exploiting light-matter interaction in silicon photonics for biosensing," Physics Seminar Series, Sewanee The University of the South, Sewanee, TN, Mar. 2017. (Invited)

T. Cao, Y. Zhao, and S. M. Weiss, "A smartphone compatible colorimetric biosensing system based on porous silicon," SPIE Photonics West, San Francisco, CA, Jan. 2017.

S. M. Weiss, G. A. Rodriguez, Y. Zhao, T. Cao, Y. M. Graham, and G. Gaur, "Resonant photonic structures in porous silicon for biosensing," SPIE Photonics West, San Francisco, CA, Jan. 2017.

S. M. Weiss, "Exploiting light-matter interaction in silicon photonics for biosensing," IEEE Photonics Society Seminar Series, University of Texas at Austin, Austin, TX, Nov. 2016. (invited)

S. M. Weiss, "Exploiting light-matter interaction in silicon photonics for biosensing," IEEE Photonics Society Seminar Series, University of Texas at Arlington, Arlington, TX, Nov. 2016. (invited)

Y. Zhao, T. Cao, G. Gaur, P. E. Laibinis, and S. M. Weiss, "Flow-through porous silicon membranes for optical biosensing," Materials Research Society Fall Meeting, Boston, MA, Nov. 2016.

Y. M. Graham, Y. Zhao, G. Gaur, and S. M. Weiss, "Low cost portable biosensors made from porous silicon annular Bragg resonators," Council on Undergraduate Research's Research Experiences for Undergraduates Symposium, Arlington, VA, Oct. 2016.

S. M. Weiss, "Exploiting light-matter interaction in silicon photonics for biosensing," IEEE Photonics Society and Materials Research Laboratory Seminar Series, University of Illinois at Urbana–Champaign, Urbana, IL, Sept. 2016. (invited)

S. M. Weiss, "Advanced photonic structures in porous silicon," 1st International Symposium on Functional Porous Materials, San Luis Potosí, Mexico, April 2016. (invited)

Y. Zhao, G. Gaur, T. Cao, P. E. Laibinis, and S. M. Weiss, "Flow-through porous silicon membranes for rapid, label-free biosensing," Porous Semiconductors – Science and Technology Conference, Tarragona, Spain, Mar. 2016. [Note: Y. Zhao received the Best Talk of the Day award for this presentation]

S. M. Weiss, “Silicon photonics for sensing,” Interdisciplinary Distinguished Seminar Series, North Carolina State University, Raleigh, NC, Oct. 2015. (invited)
K. J. Miller, G. A. Rodriguez, Y. Zhao, P. Markov, S. Hu, and S. M. Weiss, “Biosensing and optical modulation on a silicon platform,” Center for Nanophase Materials Sciences Annual Users Meeting, Oak Ridge National Laboratory, Oak Ridge, TN, Sept. 2015.
S. M. Weiss, “Nanostructured silicon biosensors,” SPIE Optics & Photonics, San Diego, CA, Aug. 2015. (invited)

Outreach:
August 2017 – Solar Eclipse event at Harpeth Hall: STEM demonstrations for middle and high school girls and community members
February 2016 - Harpeth Hall Engineering Day: Panel discussion and demonstrations for 7th grade girls at Harpeth Hall school.
March 2016 - STEM demonstrations for Metro Nashville girls
June 2015, 2016, and 2017 - Laboratory tour and demonstrations for diverse students in Tennessee Governor's School for Emerging Technologies
June 2015, 2016, and 2017 - Presentation and demonstrations for diverse students in Vanderbilt's Summer Science Academy in Nanotechnology

Honors and Awards: PI, Sharon Weiss, named Fellow of OSA (2018)
PI, Sharon Weiss, named Fellow of SPIE (2018)
PI, Sharon Weiss, named Cornelius Vanderbilt Endowed Chair in Engineering (2017)
Participating undergraduate student, Crystal Nattoo, won a best poster award for her poster at the Vanderbilt Research Experience for Undergraduates Poster Session (2017)
PI, Sharon Weiss, named an IEEE Photonics Society Distinguished Lecturer for 2016-2017
PI, Sharon Weiss, awarded the 2016 Vanderbilt School of Engineering Excellence in Teaching Award
PI, Sharon Weiss, named an inaugural Vanderbilt Chancellor Faculty Fellow for 2015-2017
Participating graduate student, Yiliang Zhao, awarded Best Talk of the Day for her presentation at the Porous Semiconductors – Science and Technology Conference in Tarragona, Spain (2016)
Participating undergraduate student, Yasmin Graham, won a best poster award for her poster at the Vanderbilt Research Experience for Undergraduates Poster Session (2016)

Protocol Activity Status:

Technology Transfer: T. Cao, S. M. Weiss, and Y. Zhao, “A smartphone compatible biosensing platform,” US Provisional Patent Application Number 62/452,773 (filed Jan. 2017)

Cooperative agreement in place effective September 1, 2018, to enable collaborative research with Adelphi Laboratory Center, US Army Research Laboratory, to carry out to integrate peptide-based protein capture agents with porous silicon biosensors. This collaborative research resulted from positive interactions during a visit to ARL in May 2017 hosted by Dr. Dimitra Stratis-Cullum and Dr. Matt Coppock.

PARTICIPANTS:

Participant Type: PD/PI
Participant: Sharon M Weiss
Person Months Worked: 1.00 **Funding Support:**
Project Contribution:
International Collaboration:
International Travel:
National Academy Member: N
Other Collaborators:

Participant Type: Postdoctoral (scholar, fellow or other postdoctoral position)
Participant: Moinul H Choudhury
Person Months Worked: 4.00 **Funding Support:**
Project Contribution:
International Collaboration:

International Travel:
National Academy Member: N
Other Collaborators:

Participant Type: Graduate Student (research assistant)
Participant: Tengfei Cao
Person Months Worked: 9.00 **Funding Support:**
Project Contribution:
International Collaboration:
International Travel:
National Academy Member: N
Other Collaborators:

CONFERENCE PAPERS:

Publication Type: Conference Paper or Presentation **Publication Status:** 1-Published
Conference Name: SPIE BiOS
Date Received: 31-Aug-2017 Conference Date: 31-Jan-2017 Date Published: 22-Feb-2017
Conference Location: San Francisco, California, United States
Paper Title: A smartphone compatible colorimetric biosensing system based on porous silicon
Authors: T. Cao, Y. Zhao, S. M. Weiss
Acknowledged Federal Support: **Y**

Publication Type: Conference Paper or Presentation **Publication Status:** 1-Published
Conference Name: SPIE BiOS
Date Received: 15-Aug-2018 Conference Date: 30-Jan-2017 Date Published:
Conference Location: San Francisco, California, United States
Paper Title: Resonant photonic structures in porous silicon for biosensing
Authors: Yiliang Zhao, Gilberto A. Rodriguez, Yasmin M. Graham, Tengfei Cao, Girija Gaur, and Sharon M. Weis
Acknowledged Federal Support: **Y**

DISSERTATIONS:

Publication Type: Thesis or Dissertation
Institution: Vanderbilt University
Date Received: 31-Aug-2017 Completion Date: 5/12/17 9:20PM
Title: Engineering porous silicon photonic structures towards fast and reliable optical biosensing
Authors: Yiliang Zhao
Acknowledged Federal Support: **Y**

FINAL REPORT: Scientific Progress and Accomplishments

ARO Project W911NF-15-1-0176

"Molecule-Surface Dynamics in Functionalized Mesoporous Silicon"

PI: Sharon Weiss, Vanderbilt University

May 1, 2015 – April 30, 2018

The primary goal of this project was to advance our understanding of the impact of functionalization chemistry and morphology on the surface interaction mechanisms involved in macroscopic diffusion and attachment of different chemical and biomolecular species in nanoscale porous films and membranes. A multitude of significant accomplishments resulted from this project, as described by scientific publication and presentations as well as through earlier progress reports. In this document, several key highlights are discussed.

(1) Understanding analyte transport and reaction in open- and closed-ended porous materials

In all of our work, we used the porous silicon material system due to its ease of fabrication by electrochemical etching, compatibility with a variety of surface chemistries, straightforward control of pore size and refractive index, and compatibility with traditional silicon processing techniques that enable the formation of on-chip porous silicon membrane structures. Both finite element simulations (COMSOL) and experiments were carried out to investigate the infiltration and binding dynamics of molecules in porous silicon films and membranes. Figure 1 shows images of one of the fabricated porous silicon structures used in this work. Figure 2a illustrates the primary challenge when using closed-ended porous materials for sensing applications for which the pore diameter is not substantially larger than the molecule size, and Figure 2b illustrates how the use of open-ended porous materials can provide a solution. The simulation results shown in the figure are based on calculations of the velocity profile under the assumption of 2D laminar flow and calculations of the concentration distribution of analyte solution using the Navier-Stokes and convection-diffusion equations. The two schemes considered are: (1) "flow-over" in which analyte flows in a microfluidic channel on top of a closed-ended porous film and infiltrates the pores through a diffusion process, and (2) "flow-through" in which analyte is forced to flow through an open-ended porous membrane, resulting in enhanced mass transport. For the flow-over scheme, the convective flow is fastest in the center of the

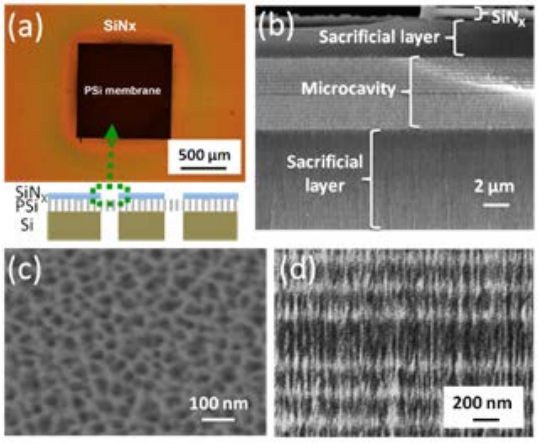

Figure 1. (a) Optical microscope image and schematic of porous silicon membrane surrounded by silicon nitride. (b) Cross-sectional SEM image of edge of membrane region showing the sacrificial layers, porous silicon layers comprising the microcavity, and remaining silicon nitride film. (c) Top view SEM image of porous silicon membrane region. (d) Magnified cross-sectional SEM image of microcavity region. Adapted from [1].

microfluidic channel and slowest at the channel edges, and the concentration distribution shows that a depletion zone forms near the porous silicon sensing region. As a result, most analytes flow downstream in the micro-channel without reaching or interacting with the porous silicon surface. In contrast, in the flow-through scheme, convective flow is strong in each pore, which provides analyte transport to receptors immobilized along the pore walls. The enhanced analyte transport in the flow-through scheme is further confirmed by the absence of a depletion zone and the lack of lateral variations in the concentration distribution plot.

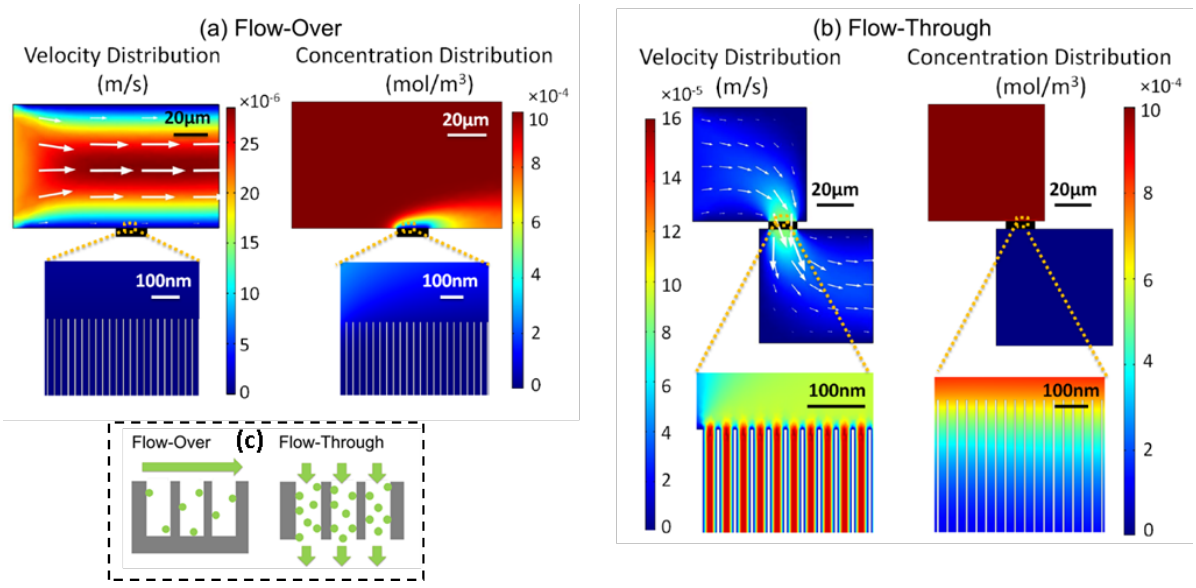

Figure 2. Velocity distribution and analyte concentration distribution at 180 s into the COMSOL simulation for (a) the flow-over scheme and (b) the flow-through scheme for porous materials. Open-ended pores facilitate significantly improved mass transport inside the porous material compared to closed-ended pores. (c) Schematic of closed-ended pores in flow-over scheme and open-ended pores in flow-through scheme. The following parameters were used in the simulations: analyte concentration c = 1 μM, diffusivity D = 10 $\mu m^2 s^{-1}$ flowed at 2 μL/min through the channel, and association constant of $k_a = 1\times10^4$ $m^3 mol^{-1} s^{-1}$ to represent high affinity binding reactions. Adapted from [1].

Analyte size plays an important role in the transport of species within porous matrices. The transport of large molecules within porous materials is slower than in bulk solution due to hindered diffusion in nanoscale pores. The equilibrium times (i.e., the time when all available sites on the sensor surface have been occupied by analytes and the sensor response reaches saturation) for porous sensors having closed-ended pores in the flow-over scheme and open-ended pores in the flow-through scheme was investigated for analytes with different diffusivities and adsorption kinetics, as shown in Figure 3. We assume a fixed flow velocity of 5 μL/min in which neither flow scheme is reaction-limited nor diffusion-limited. Although the inverse dependence of equilibrium time on adsorption rate constant is clearly shown, the time to reach equilibrium does not show a strong dependence on the adsorption rate constant due to hindered diffusion in nanopores. We find the benefit of the flow-through scheme is less significant for small analytes (i.e., molecular weight < 1 kDa) with diffusivities on the order of 10^{-9} m^2/s because their small molecular size provides relatively fast diffusive transport rate in both systems. For analytes with bulk diffusivities around 10^{-10} m^2/s, the flow-through configuration provides less than 3-fold improvement in simulated

equilibrium times compared to the flow-over scheme. When applied to larger analytes (i.e., > 100 kDa) with slow diffusivities around 10^{-11} m^2/s, the flow-through scheme shows ≈ 5 times faster equilibrium time than the flow-over scheme. For those large analytes, the flow-through configuration offers significant benefit of enhancing the mass transport efficiency by providing convective transport of analytes through the open-ended pores.

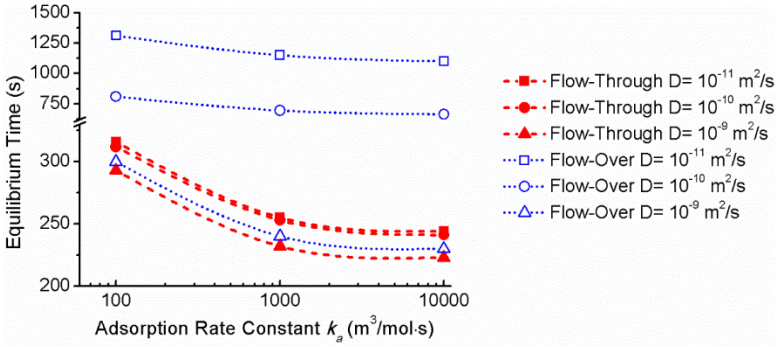

Figure 3. Equilibrium time of both flow schemes for analytes with different diffusivities D and adsorption rate constants k_a. The following parameters were used in the simulations: analyte concentration = 1 μM and fixed flow velocity of 5 μL/min. Adapted from [2].

Experimental confirmation of the simulation results was obtained by comparing the performance of flow-over and flow-through porous silicon microcavity sensors upon exposure to analytes with different sizes. 3-aminopropyltriethoxysilane (3-APTES), horseradish peroxidase (HRP), and catalase (CAT) are employed as representative analytes for their different molecular sizes and varied diffusivities in the range of 10^{-9} – 10^{-11} m^2/s. Figure 4 shows that the open-ended porous silicon microcavity membrane exhibited a 4-fold faster response when exposed to the large, 247.5 kDa CAT protein, as the flow-through scheme facilitated improved mass transport. For the adsorption of smaller molecules – 3-APTES (221 Da) and HRP (44 kDa) – little to no sensor performance improvement was observed because the closed-ended porous silicon microcavities did not suffer significant mass transport challenges with these molecules. The experimental results indicate that the flow-through porous silicon membrane is most beneficial for analysis of analytes that can enter the pores but with relatively large dimensions such as antibodies, large proteins, and long nucleic acids. Those molecules, whose diffusivities are on the order of 10^{-11} m^2/s, also exhibit the greatest improvement ratio by the flow-over format to the flow-through format in their simulated equilibrium times.

The key findings from this set of experiments are the need to appropriately tune both the pore size to molecule size ratio and to use open-ended porous silicon membranes in biosensing applications that require the detection of diffusion-limited molecules in a nanoscale porous sensor. Moreover, the simulations shown above and detailed in our publications [1-2] provide a framework to evaluate other porous sensor systems and a means to benchmark the expected performance of a porous sensor when used under various conditions of flow scheme, flow-rate, molecular concentration, molecular diffusivity, and molecular adsorption rate constant.

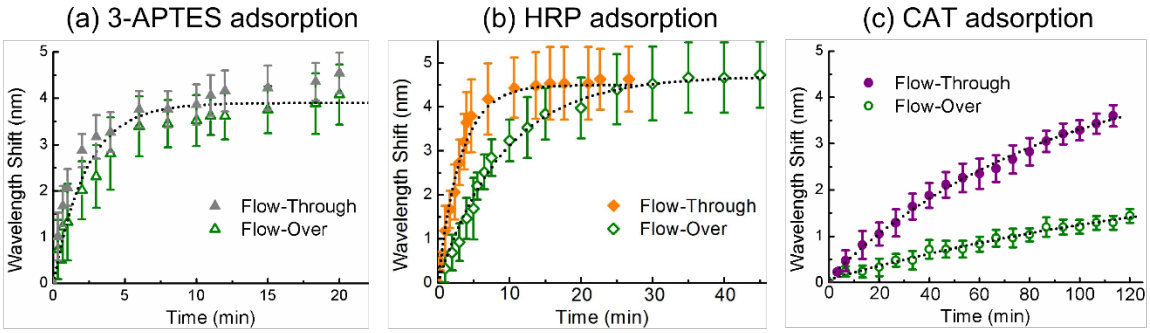

Figure 4. Time-dependent porous silicon microcavity resonance wavelength shifts upon exposure to (a) 3-APTES, (b) HRP, and (c) CAT. Solid symbols are experimental data obtained from an open-ended, flow-through porous silicon microcavity membrane; hollow symbols are experimental data from a closed-ended flow-over porous silicon microcavity. Dotted lines provide guides to the eye. Adapted from [2].

(2) Surface passivation of porous silicon for biosensing applications using porous silicon

Our prior work [3] along with that of other groups [4] has shown that corrosion of porous silicon films fabricated from p-doped silicon occurs when the films are exposed to solutions containing negative charges. The key to overcoming the corrosion issue is to either mitigate the negative charge, for example through the use of neutrally-charged PNA probe molecules when detecting negatively charged DNA target molecules [3], or to ensure that the porous silicon surface is sufficiently passivated, for example through the use of carbon-based surface chemistry [5]. We investigated a simple tube furnace thermal carbonization approach, which is scalable and does not require sophisticated chemistry, for its potential to provide improved surface passivation against corrosion for diverse applications including DNA sensing. Earlier work suggests that thermally carbonized porous silicon films can be more resilient against corrosion compared to porous silicon films that are hydrosilylated with undecylenic acid [6], but to date there have been very few reports of using thermally carbonized porous silicon films for sensing applications, and no reports on thermally carbonized porous silicon films for the detection of negatively charged DNA.

For our initial experiment, several porous silicon microcavities were first fabricated by electrochemical etching. A schematic of the microcavity and a typical reflectance spectrum are shown in Figure 5. The porous silicon microcavity is composed of 10 pairs of low (n_L = 1.3, thickness t_L = 115 nm, porosity = 90%, average pore diameter d_L = 36 nm, surface area based on cylinder model S_L = 41 cm^2) and high (n_H = 1.7, t_H = 88 nm, porosity = 63%, d_H = 17 nm, S_H = 26 cm^2) refractive index layers separated by a low refractive index cavity layer (n_L = 1.3, t_L=230 nm, porosity = 90%, d_L = 36 nm, S_L = 82 cm^2) in the center. The microcavity structure was selected for its characteristic resonance surrounded by a stopband of high reflectance. Corrosion of the porous silicon microcavity results in a resonance blueshift (i.e., spectral shift to shorter wavelength) and reduction in reflectance of the stopband. The amount of carbonization of the microcavity can also be tracked by monitoring the reflectance spectrum. Addition of material results in a reflectance redshift (i.e., spectral shift to longer wavelength). However, addition of too much carbon into the porous silicon matrix would destroy the necessary refractive index profile of the microcavity, leading to a loss of the resonance. If the resonance is lost, the high sensitivity of the structure for biosensing applications is also lost.

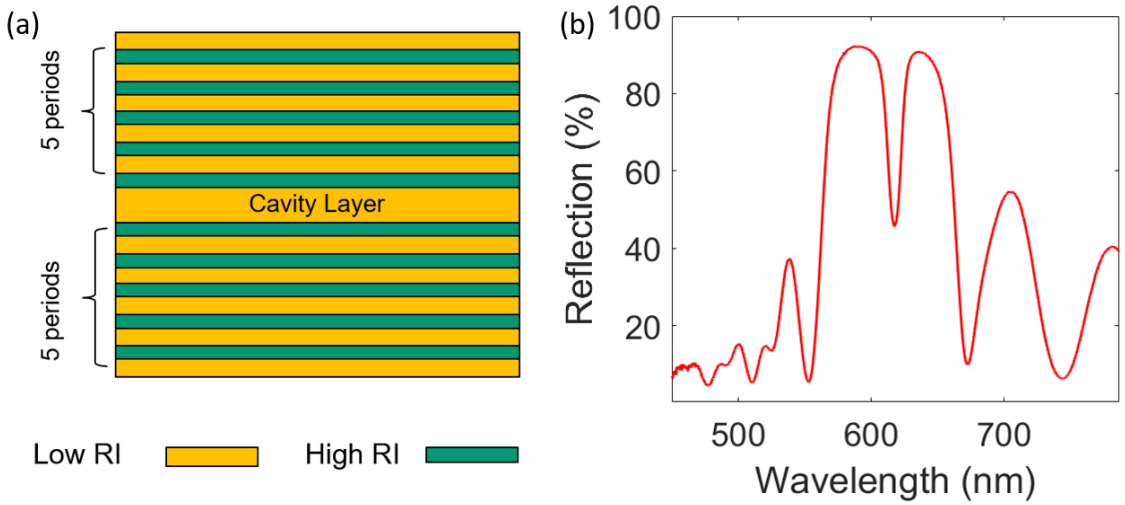

Figure 5. (a) Schematic of porous silicon microcavity used in initial thermal carbonization experiments. (b) Typical reflectance spectrum for porous silicon microcavity, characterized by resonance dip in the middle of a spectral region of high reflectance. The resonance wavelength changes when material is added or removed from the porous silicon microcavity.

The porous silicon microcavities were placed in different locations along the length of a tube furnace to provide a simple method of sweeping the temperature exposed to the samples and, therefore, modifying the amount of carbon grown on each sample. The samples were massed before and after carbonization to estimate the amount of carbon growth. To achieve thermal carbonization, a $C_2H_2/H_2/Ar$ gas mixture was flowed in the furnace and the temperature was ramped from 650˚C to 850˚C, following a previously developed recipe [7]. Briefly, the deposition was carried out in a vacuum of a few mTorr with 1 SLM of Ar and 200 SCCM of H_2. When the furnace reached 650˚C, 10 SCCM of C_2H_2 was added and the temperature was ramped up to 750˚C. The temperature was held at 750˚C for 10 minutes before being increased to 850˚C and held for another 10 minutes. Then the C_2H_2 was turned off and the sample was cooled in the furnace before being removed. Figure 6 shows the mass density of carbon grown on the porous silicon microcavities as a function of position in the tube furnace. As expected, samples in the center of the furnace that are exposed to the highest temperatures have the most carbon. Raman measurements were carried out to confirm the presence of carbon on the samples. Figure 7 shows a typical Raman spectrum of a carbonized porous silicon microcavity exhibiting the expected peaks characteristic of defective graphene materials near 1316 cm^{-1} and 1600 cm^{-1}, which correspond to the D-band and G-band, respectively [7].

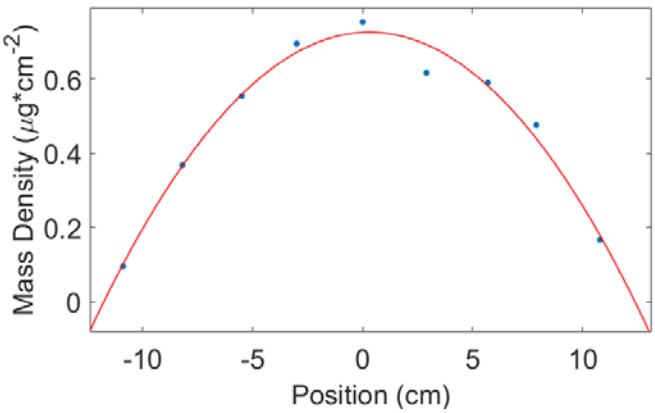

Figure 6. Mass density of carbon grown on porous silicon microcavity (e.g., mass per unit internal surface area of the porous silicon microcavity) as a function of position in the tube furnace. Samples in the center of the tube had the more carbon than samples at the edge of the furnace.

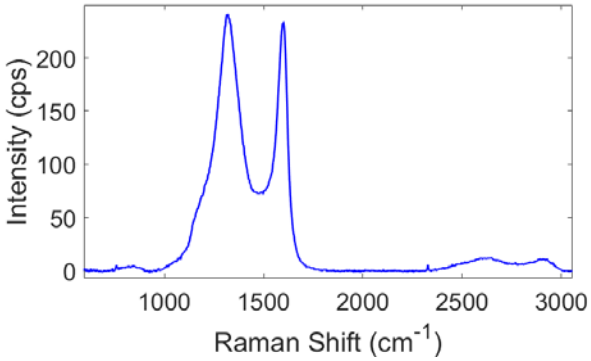

Figure 7. Raman spectrum of thermally carbonized porous silicon microcavity. The D-band (near 1316 cm^{-1}) and G-band (near 1600 cm^{-1}) peaks confirm the presence of carbon on the sample.

In order to evaluate the robustness of the porous silicon microcavities to solutions containing negative charges, the microcavities were exposed to an aggressive 50 mM solution of potassium hydroxide (KOH) with pH = 12 and their reflectance spectra were monitored at different time points. To provide a reference, an as-anodized porous silicon microcavity (i.e., freshly etched with hydrogen termination on the surface) and a thermally oxidized porous silicon microcavity were also exposed to the KOH solution. Figure 8a shows that the as-anodized sample experiences rapid corrosion, resulting in removal of the porous silicon microcavity in about 1 hour. While passivation by thermal oxidation maintains a high quality reflectance spectrum, it provides little protection against corrosion in the basic solution (Figure 8b). After 1 hour, the resonance shifts by about 25 nm, which is significant and would preclude accurate biosensing measurements without further surface passivation, and after 2 hours, the resonance can no longer be measured. Figure 8(c,d) shows the reflectance spectra for two of the thermally carbonized samples: one from the center of the furnace, and one from the edge. There is a tradeoff between the optical properties and anti-corrosion properties of the carbonized samples. Higher levels of carbonization provide excellent surface passivation and protection again corrosion in basic solutions, but compromise the optical properties of the microcavity to an extent that the characteristic resonance is no longer measurable and the reflectance intensity is significantly reduced (Figure 8c). On the other hand, lower levels

of carbonization maintain the desired high quality microcavity resonance, but likely do not provide complete surface passivation of the very high surface area, dendritic pores, allowing some degree of corrosion in basic solutions (e.g., 2.6 nm resonance shift shown in Figure 8d).

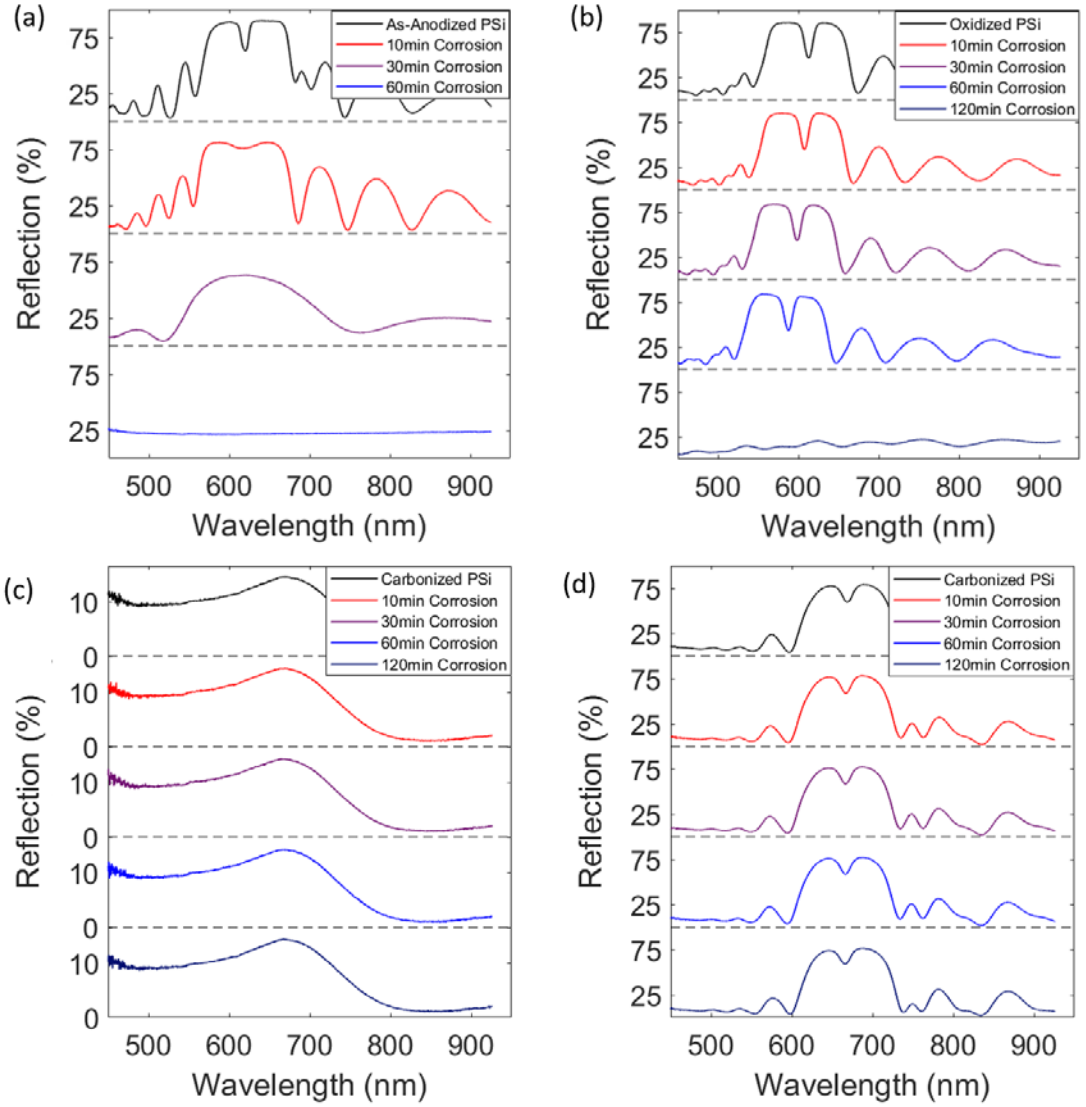

Figure 8. Reflectance spectra of (a) as-anodized and (b) thermally oxidized porous silicon microcavity exposed to a 50 mM KOH solution for varying amounts of time. Both microcavities are rapidly corroded, and the resonance is lost in less than 2 hours incubation in the basic solution. Reflectance spectra of thermally carbonized porous silicon microcavity with (c) 0.75 μg/cm^2 of carbon (center of tube furnace) and (d) 0.17 μg/cm^2 of carbon (edge of tube furnace) exposed to same KOH solution. More carbonization leads to a loss of the resonance and significantly reduced reflection intensity while the lower degree of carbonization allows a small amount of corrosion (i.e., 2.6 nm shift after 2 hrs in basic solution).

We next investigated the performance of thermally carbonized porous silicon films for DNA sensing. For this study, we chose to employ single layer porous silicon films with larger pores to minimize diffusion and mass transport issues that could arise from the use of the films with closed-ended pores [1, 2]. Figure 9 shows images of the single layer porous silicon film with an average

pore diameter of 75 nm and thickness of 3.65 μm. We compared the DNA sensing results on thermally carbonized single layer films with those on oxidized single layer films. Due to the different surface terminations, different surface chemistry was required to attach DNA probes on the thermally carbonized samples compared to the oxidized samples, as discussed below.

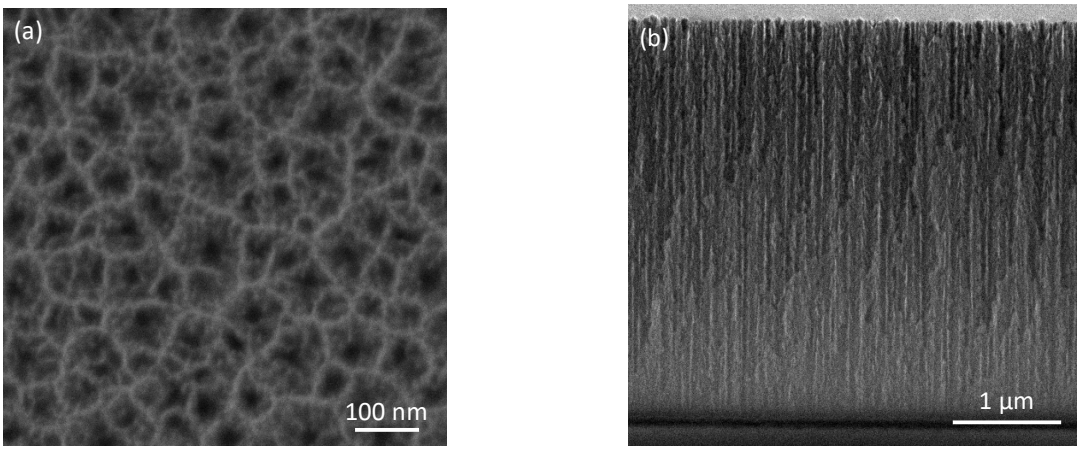

Figure 9. (a) Top view and (b) cross-sectional SEM images of single layer porous silicon film prepared in same manner as those used in the DNA sensing experiments to investigate the influence of surface passivation approaches.

For the oxidized samples, we followed our previously established protocol. Oxidation was carried out in an oven in an ambient air environment at 500 °C for 30 min. Then, a 4% 3-APTES solution in methanol and deionized (DI) water was placed on the oxidized samples for 15 min, followed by a 15 min soak in methanol to remove unbounded molecules. Next, the samples were thermally annealed for 10 min at 150 °C in air and rinsed with methanol. A 4.0 mg/mL solution of succinimidyl 3-(2-pyridyldithio)propionate (SPDP) in ethanol was placed on 3-APTES modified surface for 30 min, followed by a 30 min soak in ethanol. A 100 μM solution of thiol-modified 16-base probe DNA (5'-TAG CTA TGG TCC TCG T-3') in 4-(2-hydroxyenthyl)-1-piperazineethanesulfonic acid (HEPES) buffer (pH = 7.2) was reduced by 0.1 M tris(20carboxyethyl)phosphine disulfide reducing gel (TCEP) for one hour and the solution was vortexed intermittently for 20 s. To separate TCEP from the DNA solution, 3 M sodium acetate solution was added to the solution containing DNA and left in the freezer (-20°C) for 20 min. Then the solution was centrifuged at 12,000 rpm for 10 min, which formed a white DNA pellet at the bottom of the centrifuge tube. The supernatant was decanted and the pellet was washed with anhydrous ethanol and dried in air. Finally, HEPES buffer was added to the DNA pellet and vortexed. The DNA solution was drop casted on the SPDP functionalized porous silicon and the samples were incubated for one hour. The samples were then soaked in HEPES buffer for 15 min and rinsed with DI water. To demonstrate specific molecular detection, the probe DNA-functionalized, oxidized porous silicon samples were soaked in 10 μM complementary target DNA (ACG AGG ACC ATA GCT A) in HEPES buffer for one hour followed by rinsing in HEPES buffer and then an additional 15 min soak in HEPES buffer. Finally, the samples were rinsed with DI water to ensure that no salts remained on the samples. Figure 10a shows the reflectance measurements on the oxidized porous silicon sample after each functionalization step and after attachment of the target DNA. To more clearly distinguish the spectral shifts of the Fabry-Perot

fringes, a fast Fourier transform (FFT) of the reflectance data was taken using a Hamming window to determine the effective optical thickness of the porous silicon, as shown in Figure 10b. The effective optical thickness is defined as $2nL$ where n is the refractive index of the material and L is the thickness of the material. Hence, with knowledge of the film thickness from the SEM in Figure 9b (3.65 μm), we can directly track the change in effective refractive index of the porous silicon film after attachment of the different molecules. After addition of each of the 3-APTES, SPDP, and probe DNA molecules, there is a corresponding redshift that verifies molecules are attached to the porous silicon. However, after attachment of the complementary DNA target, a 1.36 nm blueshift results (corresponding to a refractive index change of approximately -0.003), confirming the corrosion effect previously reported [3].

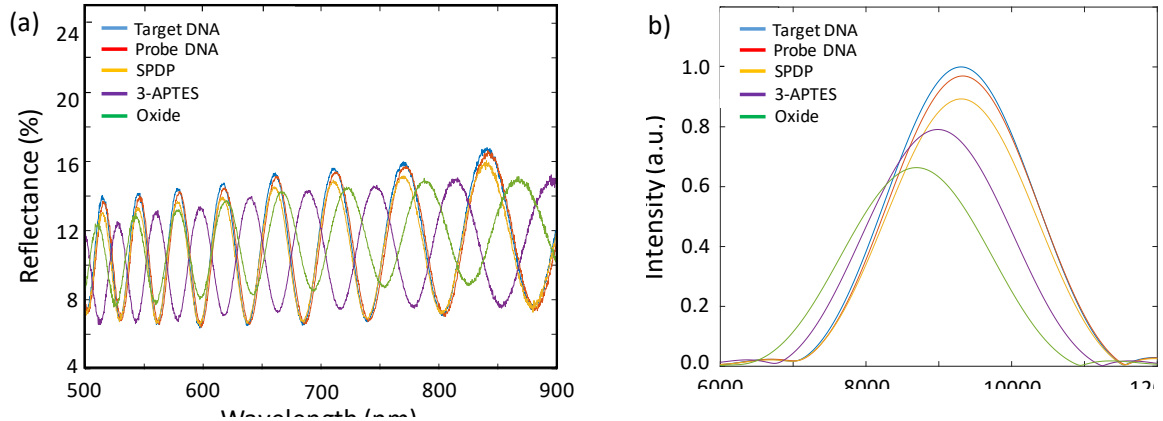

Figure 10. (a) Reflectance spectra oxidized porous silicon single layer sample after each functionalization step and after exposure to target DNA. (b) Fourier transform of the reflectance spectra in (a) revealing the effective optical thickness (2nL) of the sample at each step. A redshift and increase in effective optical thickness results from attachment of 3-APTES, SPDP, and probe DNA, confirming addition of those molecules. Although the complementary target DNA hybridized to the probe DNA, the small redshift that should results from the molecular attachment is overwhelmed by the corrosion of the porous silicon film when the negative charges destructively interact with the surface and cause a larger blueshift and reduction in effective optical thickness.

For the thermally carbonized samples, we followed protocol discussed earlier in this section to thermally carbonize single layer porous silicon samples at a position of 10 cm from the center of the tube furnace. Then, a carboxylic acid terminated porous silicon surface was achieved using a sebacic acid solution that was bubbled in argon gas for 30 min before exposure to the carbonized porous silicon samples for 2 hours at 75°C. After the reaction, the samples were washed with ethanol and acetone, and dried with nitrogen gas. Next, the samples were incubated in an aqueous solution of 0.4 mM EDC and 0.1 mM NHS for 1 hour at room temperature, followed by rinsing with DI water and ethanol and drying with nitrogen. A 90 μM solution of amine-modified 16-base probe DNA (5'-TAG CTA TGG TCC TCG T-3') in 4-(2-hydroxyenthyl)-1-piperazineethanesulfonic acid (HEPES) buffer (pH = 7.2) was added to the samples and incubated for 1 hour. The samples were then washed and left in HEPES buffer for 15 min after which time the samples were washed with DI water and dried with nitrogen. To demonstrate specific molecular detection, the probe DNA-functionalized, thermally carbonized porous silicon samples

were soaked in 10 μM complementary target DNA (ACG AGG ACC ATA GCT A) in HEPES buffer for one hour followed by rinsing in HEPES buffer and then an additional 15 min soak in HEPES buffer. Finally, the samples were rinsed with DI water to ensure that no salts remained on the samples. Figure 11 shows the reflectance measurements on a thermally carbonized porous silicon sample after each functionalization step and after attachment of the target DNA. We note that the fringe contrast is reduced for the thermally carbonized porous silicon film compared to the oxidized porous silicon film, although the fringes remain clearly discernable. After addition of each of the sebacic acid, EDC/NHS, and probe DNA molecules, there is a corresponding redshift that verifies that these functionalization molecules are attached to the porous silicon. Attachment of the complementary DNA target also leads to a redshift (0.23 nm) and increase in the effective optical thickness of the porous silicon (+0.0004), suggesting that the increase in refractive index resulting from hybridization is larger than any corrosion contribution, if one exists. Since a significantly lower concentration of target DNA was used compared to probe DNA, it is expected that the fringe shift and optical thickness change resulting from target DNA attachment will be smaller than that for probe DNA attachment. Hence, it is challenging to determine whether there is any corrosion in the thermally carbonized porous silicon sample upon exposure to the target DNA. We therefore subsequently exposed the sample to a 100 μM complementary target DNA solution, and measured an additional and large 2.24 nm redshift of the Fabry-Perot fringes. Since the corrosion effect, if present, is expected to increase when the sample is exposed to more negative charge, it is unlikely that the thermally carbonized silicon experiences significant corrosion during DNA sensing experiments. Hence, we have shown that the relatively straightforward thermal carbonization approach can be used to enable effective DNA sensing using porous silicon films. We note that this work is currently being finalized for publication. The final results will include comparison to porous silicon films passivated by hydrosilylation, an alternate but more complicated approach to achieving silicon-carbon surface bonds.

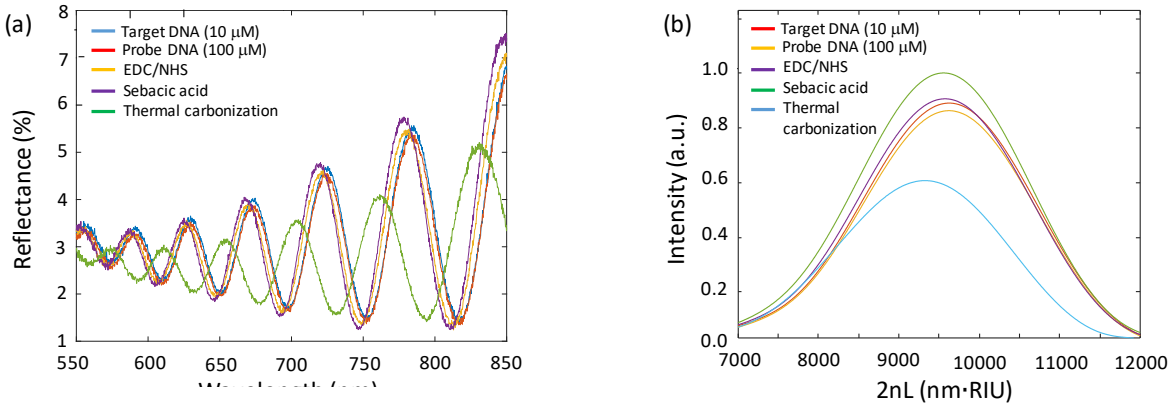

Figure 11. (a) Reflectance spectra thermally carbonized porous silicon single layer sample after each functionalization step and after exposure to 10 μM target DNA. (b) Fourier transform of the reflectance spectra in (a) revealing the effective optical thickness (2nL) of the sample at each step. A redshift and increase in effective optical thickness results from attachment of 3-APTES, SPDP, and probe DNA, confirming addition of those molecules. Hybridization of the complementary target DNA also leads to a redshift, confirming that the corrosion process observed in the oxidized porous silicon film is mitigated with the carbon surface passivation.

(3) Use of smartphone for portable, low-cost biosensing using porous silicon films: detection of structural color changes that result from molecule capture events

For all optical measurements in the aforementioned experiments, a commercial spectrometer and white light source were used. As an alternate measurement approach, we demonstrate the feasibility of monitoring changes in the optical properties of porous silicon films using a smartphone to replace the spectrometer and white light source. In this way, costly and large footprint measurements tools can be replaced by a highly portable measurement tool that is widely available in a multitude of environments around the world – a smartphone. The basic concept is that a spectral change measured by a spectrometer can be replaced by a color change measured by a smartphone camera. As illustrated in Figure 12, a spectral shift of a characteristic spectral feature is always accompanied by an intensity change, and this intensity change can be mapped to a color change by selecting a narrowband spectral region of the characteristic spectral feature and evaluating the intensity of that region using the red (R), green (G), or blue (B) channel of a smartphone camera. In the example in Figure 12, integrating the intensity within the highlighted grey rectangle (Figure 12a) results in an overall decrease in intensity after target molecule capture, represented as a change in the R-channel value from 250 to 150 (Figure 12b). We note that the color change is caused by a change in the porous silicon refractive index that results when analyte or molecular species infiltrate the pores; hence, the color change mechanism is distinct from traditional colorimetric sensors that require chemical reactions or incorporation of color-inducing species such as dyes.

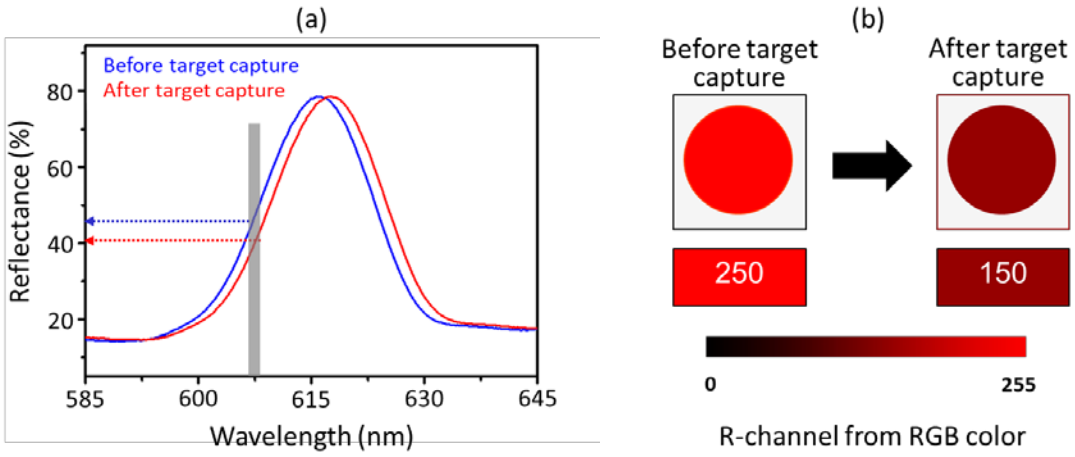

Figure 12. Basic concept of correlating spectral and color-based detection. (a) Reflectance spectrum shifts when molecules are added to a sensor. Over a selected narrowband range of wavelengths, denoted by the grey rectangle, the spectral shift produces an intensity change. (b) R-channel value of smartphone camera quantifies intensity of "red" color in a particular image. In the spectrum shown in (a), molecule capture results in a decrease in intensity of light in the R-channel and therefore a lower R-channel value.

For initial proof-of-concept testing, we characterized a porous silicon sensor using an optical microscope equipped with a digital camera [8]. The porous silicon sensor we used was a porous silicon rugate filter composed of 60 alternating layers of low (n_L = 1.5, porosity = 82%, thickness t_L = 100 nm) and high (n_L = 1.6, porosity = 76%, thickness t_L = 95 nm) refractive index layers, as shown schematically in Figure 13. The center wavelength of the rugate filter is in the red part of the spectrum near 600 nm and the full-width-at-half-maximum is 20 nm. When analytes infiltrate into the pores of the rugate filter, the effective refractive index of the porous silicon layers increase, causing the peak reflectance wavelength of the rugate filter to shift to higher wavelengths. To facilitate color-based detection, a narrow bandwidth, 10 nm FWHM bandpass filter with peak transmittance at 610 nm was also utilized in the measurement system. This bandpass filter transforms spectral shifts, for example due to molecular attachment in the pores, into intensity changes, which can be detected by a camera. Figure 14a illustrates the sensing principle when glucose solutions of various concentrations are exposed to a porous silicon rugate filter. As the concentration of the glucose solution increases, the reflection spectrum of the rugate reflector redshifts first from the left to the center of the bandpass filter region and later from the center to the right side of the bandpass filter region, corresponding to color changes from dark to bright and then bright to dark. While it is straightforward to detect a color change over this continuous spectral region, the most sensitive detection occurs at the shoulders of the bandpass filter region where the slope is steepest. Accordingly, we designed porous silicon rugate sensors to have their peak reflectance wavelength in this shoulder region before the addition of the target solution under test. To demonstrate quantitative detection, we correlated the intensity changes in the *R* (red) values of the images to wavelength shifts of the peak reflectance wavelength measured by a spectrometer. As shown in Figure 14b, a linear relationship was found between the change of red intensity in the RGB model and the wavelength shift. An algorithm was developed to remove the noise in the images, which improved both the sensitivity and reliability of the colorimetric detection. The minimum resolvable wavelength shift was less than 0.25 nm, which is comparable with the detection limit of many commercial spectrophotometers.

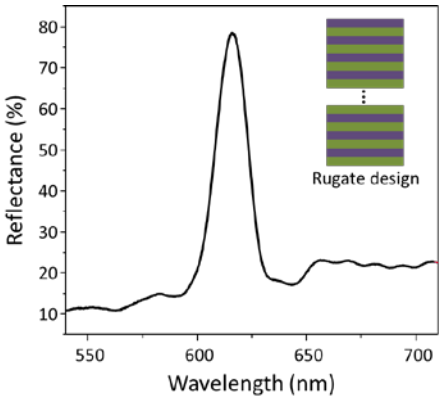

Figure 13. Reflectance spectrum of porous silicon rugate filter. Schematic of rugate filter design is shown in the inset.

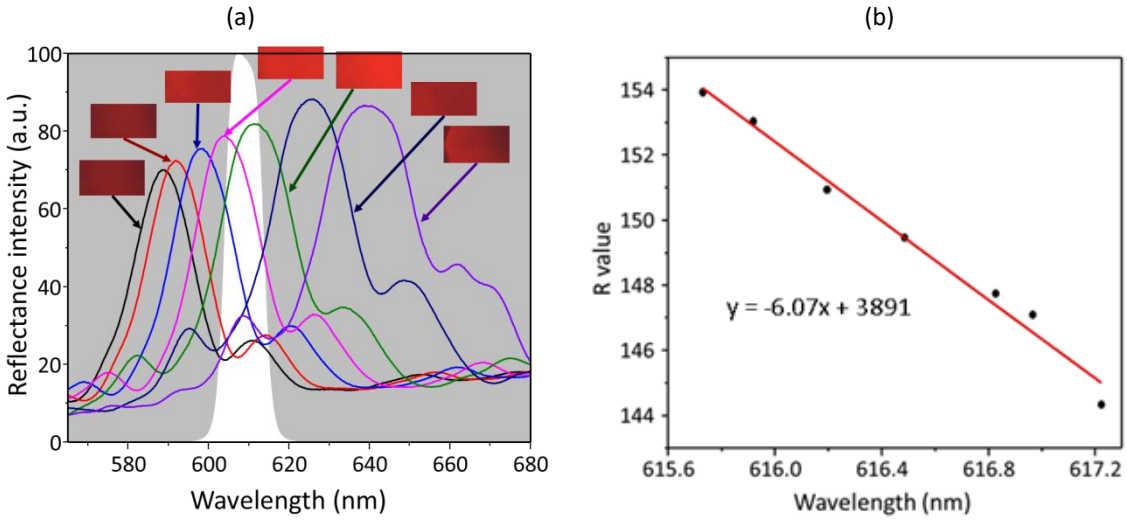

Figure 14. (a) Reflectance spectra of porous silicon rugate filter after infiltration with glucose solutions of varying concentration (increasing from left to right). The white region indicates the normalized transmission spectrum of the bandpass filter that limits the wavelength region of reflected light reaching the camera. Camera images of the porous silicon rugate filter infiltrated with the various glucose solutions are shown above each corresponding spectrum. Each image can be uniquely identified by the red (R) intensity of the RGB value. (b) Correlation of R-value intensity changes with the wavelength shift of the porous silicon rugate sensor. Adapted from [8].

We next carried out detection with a smartphone in which the light source was the camera flash and the camera was the one integrated in the smartphone, as illustrated in Figure 15. Similar to the experiment described previously with the microscope and digital camera, we carried out a sensing experiment with different concentrations of glucose solution, but this time took all data with a smartphone (iPhone SE, model A1662). Measurements with both the smartphone and an Ocean Optics spectrometer were taken after exposure of the porous silicon rugate filter to each of the different glucose concentrations. Figure 16 shows the reflection spectra measured by the spectrometer and the correlation between the peak wavelength of the rugate filter measured by the spectrometer and the *R*-channel value measured by the smartphone. We note that the two primary challenges for the smartphone measurement are the non-uniformity of the porous silicon film and the non-uniformly bright illumination by the camera flash; both of these challenges result in measurement errors when the position of the porous silicon sample changes with respect to the smartphone position. In order to mitigate these issues, care was taken to keep the porous silicon sample position fixed, to carry out averaging over 20 images for each glucose concentration, and to use a diffuser to improve the uniformity of the illumination spectrum. By comparing Figure 14b and Figure 16b, it is clear that a calibration of each camera used for the sensing experiments will be necessary before molecular quantification is possible. This calibration should be valid as long as the camera performance remains unchanged.

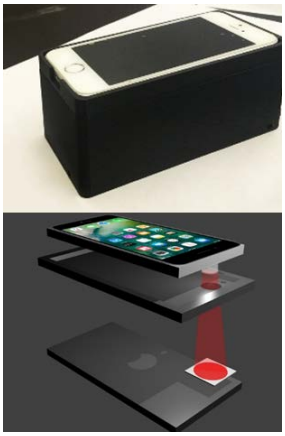

Figure 15. Photo (top) and schematic cut-away view (bottom) of porous silicon smartphone sensor with 3D printed box.

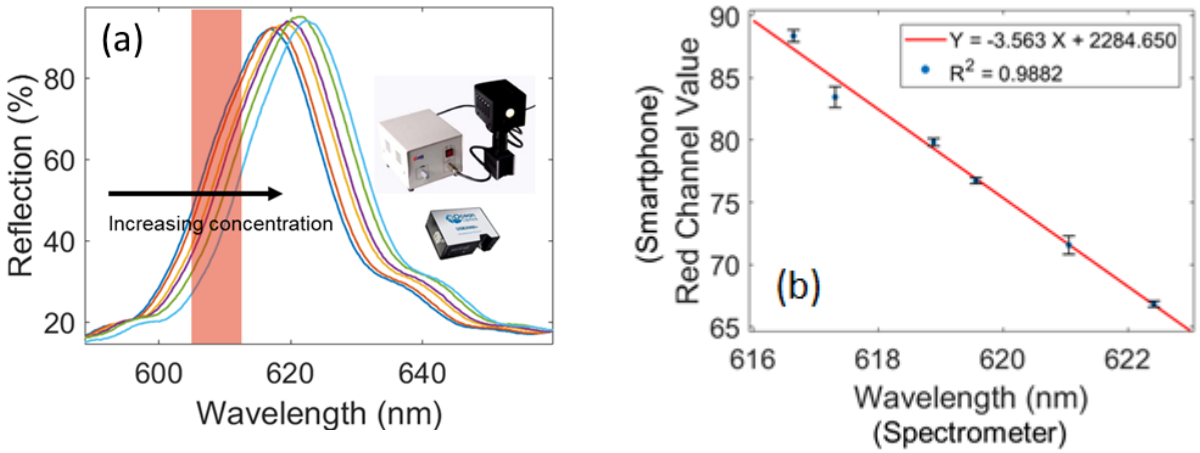

Figure 16. (a) Reflectance spectra of porous silicon rugate filter after infiltration with glucose solutions of varying concentration (increasing from left to right in the figure), as measured by Ocean Optics spectrometer. (b) Correlation between peak resonance wavelength of porous silicon rugate filter measured by the commercial spectrometer and the R-channel value measured by a smartphone for different glucose concentrations.

Finally, we report measurement of biotin-streptavidin detection using the smartphone and a porous silicon microcavity. Instead of calibrating with glucose solution, we employed a hydrolysis reaction of 3-aminopropyltriethoxysilane (3-APTES). A solution of 5% 3-APTES was dropped on the porous silicon microcavity sample and allowed to sit at room temperature for 10 min. The sample was then rinsed in hot water (~60℃) for 0, 30, 90, 150, 210, and 300 seconds. After each rinse step, the sample was rinsed with room temperature DI water, then measured with both an Ocean Optics spectrometer and smartphone (iPhone SE, model A1662). Figure 17 shows the reflectance spectra measured by the spectrometer and examples of data extracted from the smartphone. For the spectrometer measurements, the position of the highest peak of the porous silicon reflectance was chosen as the peak wavelength (always the right hand side peak of the microcavity dip). For the smartphone measurement, videos clips longer than 1 minute were taken after each rinse step. The videos were treated as a series of RGB images. *R* value matrices were calculated in Matlab by averaging over the first 5 frames of the videos for every second. Then, the area with $R \geq R_0$ was calculated, where R_0 is a selected value, and normalized with respect to the maximum of all measured intensity values. Hence, for each measurement cycle during the hydrolysis experiment, we determined the peak wavelength of the porous silicon microcavity from the spectrometer and an intensity value representing the normalized, integrated intensity within an area containing *R* values greater than 30.

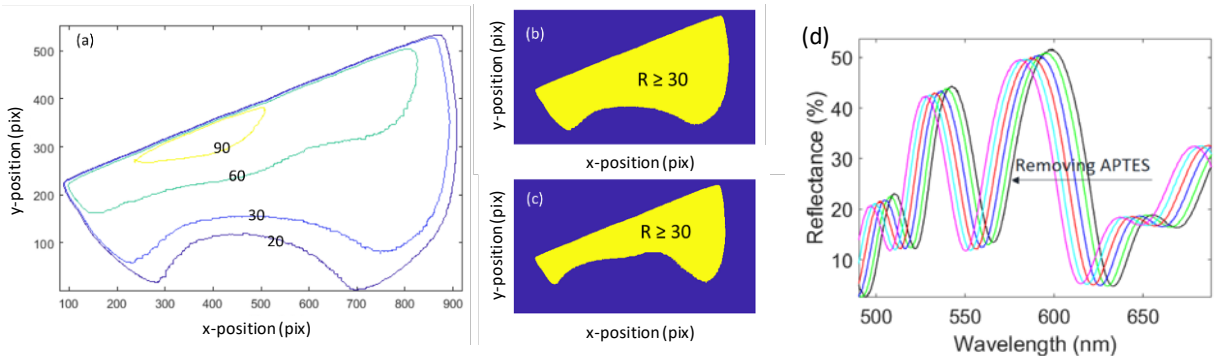

Figure 17. (a) Contour plot of video clips taken by the camera based on time-averaged R value matrix. Area of the image with R > 30 before (a) and after (b) removing 3-APTES from the porous silicon with the hydrolysis reaction. (c) Reflectance spectra of porous silicon microcavity during 3-APTES hydrolysis reaction at several time points.

Figure 18 shows the relationship between the peak wavelength (spectrometer) and normalized intensity (smartphone) with both the data points measured during the hydrolysis experiment and a calibration curve fitting those data points. The calibration curve has the following format: $I = \mathrm{C} * \sum_{\lambda} LS(\lambda) * F(\lambda) * S(\lambda + \Delta\lambda) + \Delta\mathrm{I}$ where the I is the intensity of light received at the smartphone photon detector, $LS(\lambda)$ is the emission spectrum of the light source, $F(\lambda)$is the transmittance of the filter used to restrict the wavelength range reaching the sample as discussed earlier (center wavelength = 610 nm, FWHM = 10 nm), C is the camera spectral response over the wavelength range transmitted by the filter (assumed to be constant), and $S(\lambda + \Delta\lambda)$ is the reflectance of the porous silicon microcavity. The $\Delta\mathrm{I}$ and $\Delta\lambda$ terms are introduced to account for errors that arise due to image processing and measurement of a slightly different position on the sample in the spectrometer and smartphone, respectively. The three free parameters in the above equation are C, $\Delta\lambda$, and ΔI. Very good agreement between the fit and the measured data is shown in Figure 18. Over the measured range of about 20 nm, the 3σ accuracy of the integrated R-value intensity corresponds to 0.3 nm.

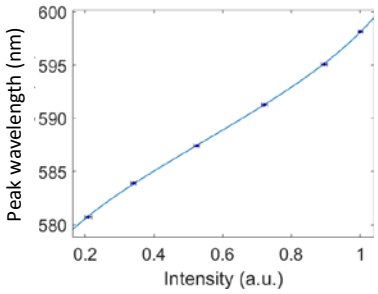

Figure 18. Calibration curve correlating data from spectrometer and smartphone. The blue dots are the 3-APTES hydrolysis data and the line is the modeled curve fit.

Figure 19 shows the results of the biotin-streptavidin assay as measured by the spectrometer and smartphone. The porous silicon microcavity sensor was prepared by functionalization with thermal oxide, 2% 3-APTES (20 min soak in 3-APTES, rinsing in methanol and PBS soak for 15 min, annealing at 150˚C in air for 30 min, 20 min soak in PBS), and 1 mg/mL Sulfo-NHS-biotin in PBS (incubated for 30 min). Then, target streptavidin molecules (50µL of 4 µM streptavidin solution) were pipetted onto the functionalized porous silicon microcavity and incubated for 30 min before rinsing. As shown in the inset of Fig. 19b, the color change resulting from streptavidin attachment is not easily discernable by eye, but is easily measured by the smartphone camera and shows good agreement with the calibration curve. This promising first demonstration of porous silicon sensing with a smartphone detection system opens the door to further investigations that leverage the advantages of high surface area nanoscale porous silicon sensors with the ubiquitous and portable smartphone measurement system.

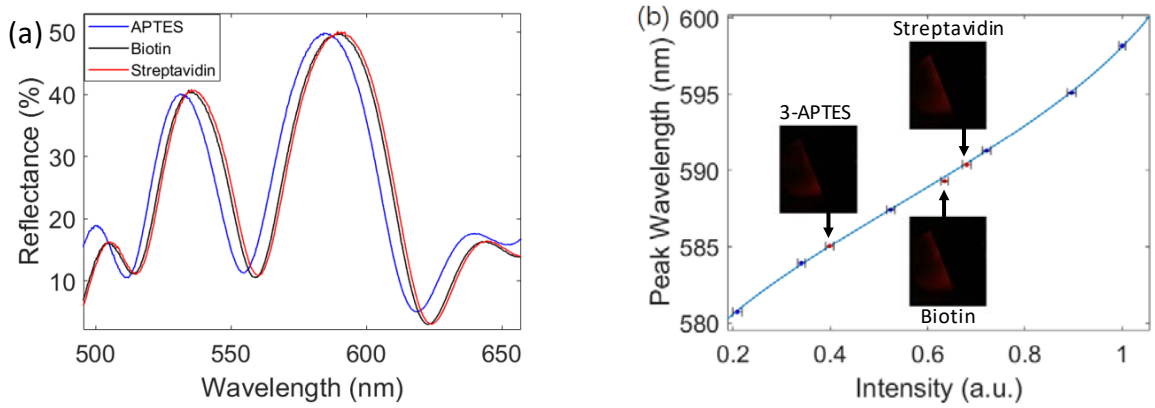

Figure 19. (a) Reflectance spectra measured by spectrometer after attachment of 3-APTES (blue), biotin (black, 4.3 nm redshift), and streptavidin (red, 1.1 nm redshift). (b) Data points corresponding to biotin-streptavidin assay (red data points) superimposed on calibration curve correlating data from spectrometer and smartphone. The blue data points from the 3-APTES hydrolysis experiment are also shown for reference. Inset shows frames from camera video after biotin and streptavidin attachment. While the color change is challenging to decipher by eye, it is easily resolvable using the smartphone and associated image processing.

References

[1] Y. L. Zhao, G. Gaur, S. T. Retterer, P. E. Laibinis, S. M. Weiss, "Flow-Through Porous Silicon Membranes for Real-Time Label-Free Biosensing," Anal Chem **88**, 10940-10948 (2016).

[2] Y. Zhao, G. Gaur, R. L. Mernaugh, P. E. Laibinis, S. M. Weiss, "Comparative kinetic analysis of closed-ended and open-ended porous sensors," Nanoscale Res Lett **11**, 395 (2016).

[3] Y. L. Zhao, J. L. Lawrie, K. R. Beavers, P. E. Laibinis, S. M. Weiss, "Effect of DNA-induced corrosion on passivated porous silicon biosensors," ACS Appl Mater Inter **6**, 13510-13519 (2014).

[4] C. Steinem, A. Janshoff, V. S. Y. Lin, N. H. Volcker, M. R. Ghadiri, "DNA hybridization-enhanced porous silicon corrosion: mechanistic investigators and prospect for optical interferometric biosensing," Tetrahedron **60**, 11259-11267 (2004).

[5] L. De Stefano, P. Arcari, A. Lamberti, C. Sanges, L. Rotiroti, I. Rea, I. Rendina, "DNA optical detection based on porous silicon technology: from biosensors to biochips," Sensors **7**, 214-221 (2007).

[6] B. Sciacca, S. D. Alvarez, F. Geobaldo, M. J. Sailor, "Bioconjugate functionalization of thermally carbonized porous silicon using a radical coupling reaction," Dalton Trans **39**, 10847-10853 (2010).

[7] L. Oakes, A. Westover, J. W. Mares, S. Chatterjee, W. R. Erwin, R. Bardhan, S. M. Weiss, C. L. Pint, "Surface engineered porous silicon for stable, high performance electrochemical supercapacitors," Sci Rep **3**, 3020 (2013).

[8] T. Cao, Y. Zhao, S. M. Weiss, "A smartphone compatible colorimetric biosensing system based on porous silicon," Proc. of SPIE **10077**, 1007713 (2017).